Received 10 July 2025; Accepted 20 November 2025
https://doi.org/10.48612/letters/2025-4-409-415
https://elibrary.ru/vhsopv

Behavior of magnesium alloy Mg-9Gd-4Y-1Zn-0.5Zr (wt.%) after different types of loading

S. A. Atroshenko[†1,2], M. N. Antonova[1,2], S. Zhao[2], L. Xu[2], R. V. Lukashov[2], Yu. V. Petrov[1,2]

[†]satroshe@mail.ru

[1]Institute for Problems in Mechanical Engineering of the Russian Academy of Sciences, Saint-Petersburg 199178, Russia
[2]Saint Petersburg State University, Saint-Petersburg 199034, Russia

Abstract: The paper examines the microstructure of a new promising rare-earth magnesium alloy Mg-9Gd-4Y-1Zn-0.5Zr (wt.%) following extrusion and directional cutting, as well as subsequent quasi-static and high-speed compression tests, including the Taylor test. This alloy is characterized by a small number of twins, usually inherent in magnesium alloys, since the mechanism of plastic deformation changes due to rare-earth-doped elements. The microstructure was studied by optical and scanning electron microscopy. Zr-rich intermetallic phases are observed, which can lead to the formation of cracks in the vicinity of the precipitates and local embrittlement of the alloy, as well as various phases. It is noted that with an increase in the strain rate, the nature of the fracture becomes increasingly brittle, as well as individual areas of melting at a strain rate of about 6000 s^{-1}. Microhardness data for samples tested at different strain rates were also obtained. Local areas of dynamic recrystallization (DRX) are observed after high-speed testing, and grain growth is also observed with increasing strain rate, which most likely indicates post-dynamic grain growth. Novel findings regarding compression behavior provide new insights into the mechanisms of plastic deformation and fracture of the alloy under study, as well as some features for future applications.

Keywords: rare-earth magnesium alloy, microstructure, static and dynamic compression tests, Taylor impact test, strength, micromechanisms of deformation and fracture

Acknowledgements: *The authors are grateful to the Resource Centers "Nanotechnology" and "Centre for Extreme States of Materials and Constructions" of the Research Park at the Saint Petersburg State University for the helpful assistance in the characterization of some samples using SEM and for the conducting static test. The part of the work (section 4) obtained by Atroshenko, Antonova and Zhao at the support of the Russian Science Foundation (RSF 22-11-00091). Petrov and Atroshenko performed part of the work relative to optical microscopy investigations with the support of the Ministry of Science and Higher Education of the Russian Federation (project 124041500007-4). Some experimental investigations under impact loads were conducted by Lukashov, Xu and Antonova in the Mega-Lab "Dynamics and Extreme Characteristics of Promising Nanostructured Materials" founded by the project (075-15-2022-1114). Authors are grateful to G. A. Volkov and Changzeng Fan for their help in obtaining high-speed tests.*

1. Introduction

Magnesium (Mg) alloys are attractive for the automotive and aerospace industries due to their low density compared to other structural metallic materials [1]. For safety and practical applications, strength and damage resistance, that is, fracture toughness percentage, are the most important properties [2–3]. However, the search for an optimal chemical composition of magnesium alloy in mechanical properties is still ongoing, since an increase in yield strength is inevitably accompanied by a decrease in fracture toughness.

Rare earth (RE) magnesium alloys doped with gadolinium (Gd), yttrium (Y), zinc (Zn) and zirconium (Zr) are of particular interest due to their high potential for applications requiring a combination of high strength and thermal stability [4]. One of the representatives of this group, the Mg-9Gd-4Y-1Zn-0.5Zr (wt.%) alloy, belonging to the Mg-RE-Zn-Zr system, is widely studied as a basis for new-generation structural materials.

After hot extrusion, the alloy structure is characterized by the predominant formation of the lamellar LPSO (long-period stacking ordered) phase, which is formed mainly along the deformation direction. These phases can exist in the form of both particles elongated in the extrusion direction and intracrystalline inclusions, especially in the case of high concentrations of Zn and rare earth elements. The presence of LPSO phases contributes to the reinforcement of the matrix, increasing the resistance to sliding and shear, which is expressed in an increase in strength characteristics. For example, in Mg-10Gd-3Y-1.5Zn-0.5Zr alloys, a continuous complex of lamellar LPSO and small SF (stacking faults) was found inside the grains, which ensures a high tensile strength even at temperatures up to 300°C [5].

Extrusion also promotes the occurrence of DRX, leading to the formation of equiaxed grains (≈1–5 μm), the size of which varies depending on the deformation conditions and preliminary heat treatment. Zr plays an additional role in recrystallization, providing nucleation of new grains and limiting their growth due to its tendency to heterogeneous distribution along grain boundaries [6].

Studies show that after extrusion, a pronounced deformation texture is observed, characterized by a basal texture where the {0001} basal planes are aligned parallel to the extrusion direction. Such a texture leads to anisotropy of mechanical properties, including differences in strength and ductility along and across the deformation direction. However, the presence of LPSO phases and a fine-grained structure partially compensates for the texture effect, promoting a uniform stress distribution [5].

The phase composition after extrusion combines α-Mg matrix, thin LPSO lamellae, and secondary phases of Mg_{24}(RE), Mg_3RE or α-Zr can also be observed as particles along the grain boundaries and within the grains [4,7]. Fracture studies revealed that at high strain rates and impact loads, the fracture mechanism becomes ductile-brittle or predominantly brittle, especially in zones with high LPSO and Zr inclusions [8].

Finally, it is important to note that the mechanical behavior of the alloy is closely related to the evolution of the microstructure during deformation. In quasi-static and dynamic tests, phenomena such as activation of twinning, localized grain refinement, nucleation and growth of microcracks predominantly along grain boundaries and inclusions of heavy phases, such as particles rich in Zr and rare earth elements, are observed [9–11].

The recently actively studied alloys of the Mg-Gd-Y-Zn-Zr system containing LPSO phases with heterogeneous bimodal structures have demonstrated good mechanical properties concerning both the yield strength and fracture toughness [12,13]. Due to the significant dependence of the solubility of Gd and Y in the solid solution of the α-Mg matrix on temperature, the degree of age-hardening can be controlled by the precipitation of the β' phase (a metastable Mg-Gd/Y precipitate) [14]. The formation of LPSO phases and γ' precipitates (metastable Mg-Gd/Y-Zn precipitates) occurs because of adding Zn atoms to Mg-Gd-Y alloys [15]. Adding Zr atoms to alloys of the Mg-rare earth elements system leads to grain refinement of the alloy, which increases its strength [16]. In this case, if we consider the viscosity of the material as a complex indicator of strength and plasticity [17,18], then the alloys of the Mg-Gd-Y-Zn-Zr system may have great potential for achieving an exceptional balance of strength and fracture toughness.

In this paper, we will study the Mg-9Gd-4Y-1Zn-0.5Zr alloy containing a heterogeneous bimodal microstructure and an LPSO phase, manufactured by hot extrusion and then cut in the direction of extrusion. The alloy is first encountered in the work [19] and the authors noted a significantly large critical elongation during static tensile tests, over 15%, and a fairly high yield strength, over 380 MPa.

Thus, the study of the microstructure after compression tests in a wide range of strain rates of the Mg-9Gd-4Y-1Zn-0.5Zr alloy after extrusion in the deformation direction allows us to better understand the relationship between the phase composition, structure, texture and deformation mechanisms, which is critical for optimizing its performance characteristics.

It is important to test the material at different speed modes, since, despite the improvement of the material properties under quasi-static deformation modes, its properties can both decrease and increase dynamically, which was noted in our studies [20–23]. We also noted the influence of the structure on the deformation characteristics [20,23], which should be taken into account when choosing the material and operating conditions in the future.

The present work examines the microstructure after compression tests, which provide insight into the material's plastic deformation capabilities. Additionally, no previous studies on this alloy's behavior under compression were identified in the literature.

2. Materials and methods

The Mg-9Gd-4Y-1Zn-0.5Zr (wt.%) alloy was produced by direct-chill casting [19], followed by homogenization treatment at 510°C for 12 h and water quenching. The alloy was then extruded into bars at 350°C with an extrusion ratio of 10 at a constant ram speed of 1 mm/s.

All experiments were carried out under compressive loading at room temperature, including the Taylor test (impact velocity 219 m/s). The quasi-static compression tests were performed using an Instron testing machine (strain rates of 0.001 and 0.1 s^{-1}) up to fracture, and the dynamic tests were performed by using the Split Hopkinson Pressure Bar (SHPB) test (strain rates from 1300 to 5970 s^{-1}). It is important to note that in the SHPB test, the specimens did not fail at strain rates below 2000 s^{-1}, as was the case for the specimen after the Taylor test, for which only visible cracks were observed. The compression axis was parallel to the extrusion direction for all tested specimens.

Regarding the size of the tested specimens, for the Taylor test, cylinders with a diameter of 8 mm and a length of 30 mm were used; for the SHPB test — 8 mm in diameter and 4 mm in length; and for static testing — 8 mm in diameter and 8 mm in length. Prior to testing, the ends of all specimens were ground.

The primary goals of the experimental design were to approach a quasi-uniaxial stress state and uniform deformation, while providing a sufficient specimen volume for subsequent microstructural characterization.

With regard to the SHPB tests, the corresponding impact velocities calculated using a laser velocimeter ranged from 3.7 m/s to 11 m/s, and the strain rates were approximately in the range of 1300 s^{-1} to 6000 s^{-1}.

The present work examines, the use of a relatively long impact bar (60 cm) effectively increased the incident pulse duration, which promoted the growth of plastic strain under loading. This setup, used in combination with the Taylor test, is particularly suitable for studying damage evolution under moderate to low strain rate conditions. Approximation formula used for strain rate calculation in Taylor tests is

$$\frac{d\varepsilon_p}{dt} = \frac{v_0}{2(L - X)}, \tag{1}$$

where v_0 — sample impact velocity, L — initial length of the sample, X — the length of the part of the specimen that did not receive residual deformations [27].

More details on the setup can be found in references [26,27].

The microstructure obtained after extrusion processing and cut in its direction was investigated using an Axio Observer Z1M optical microscope in bright field and C_DIC (Circular-polarized light Differential Interference Contrast), as well as using a Zeiss Merlin and Melytec Zeptools ZEM 18 scanning electron microscope. Metallographic studies were carried out on polished transverse and longitudinal sections after etching in aqua regia (a mixture of HNO_3 and HCl in a ratio of 1:3). The linear intercept method was used for grain size measurement (standard 5639-82) [24].

The chemical composition was studied by energy-dispersive spectroscopy (EDX) using an Oxford Instruments INCAx-act X-ray microanalysis system attached to the microscope. The microhardness was measured using a SHIMADZU HMV-G device under a load of 100 g. The proportion of the viscous component (Shear area) in the fracture of material was determined according to ASTM E436-03 [25]. The study of the fracture surface for this purpose was carried out on an Axio Observer Z1M microscope in a dark field at a magnification of 100 with the help of Axio Vision structure analyzer, as well as using a Zeiss Merlin and Melytec Zeptools ZEM 18 scanning electron microscope.

The microstructure studies covered both transverse and longitudinal sections of the specimens, including information on the fracture surfaces.

3. Results

SEM methods were used to obtain microstructure photographs of the samples after quasi-static compression tests in transverse and longitudinal directions, as well as of the initial sample after extrusion in longitudinal direction, shown in Fig. 1. In the initial state, the metallographic texture is visible in the longitudinal section along the preliminary deformation — extrusion. Microcracks are observed in the cross section of the statically deformed sample, and slip lines located at some angle relative to the compression direction are clearly visible on a pre-polished surface after compression in the longitudinal section. EDX studies have demonstrated that Zr-rich intermetallic phases are observed in individual zones near the microcracks, and even in the initial sample not subjected to mechanical testing, its mass fraction can exceed 50% (for example, in Fig. 2b).

After static tests, preserved initial eutectic components of the $Mg_5(Gd, Y, Zn) + (Mg_2Zr + ZrZn_2)$ alloy are observed, refined because of extrusion, which is shown in Fig. 3. Also, in Fig. 3b, the grain size is different — large initial eutectic grains and small ones are visible.

Under impact loading at strain rates of 1300 – 5970 s^{-1}, the alloy microstructure exhibits pronounced local grain refinement (up to ≈1 µm) in the impact zone (cross-section). The onset of crack formation was usually observed near Zr-rich intermetallic phases, as confirmed by the EDX method. At higher strain rates, nearly parallel cracks are observed. In the

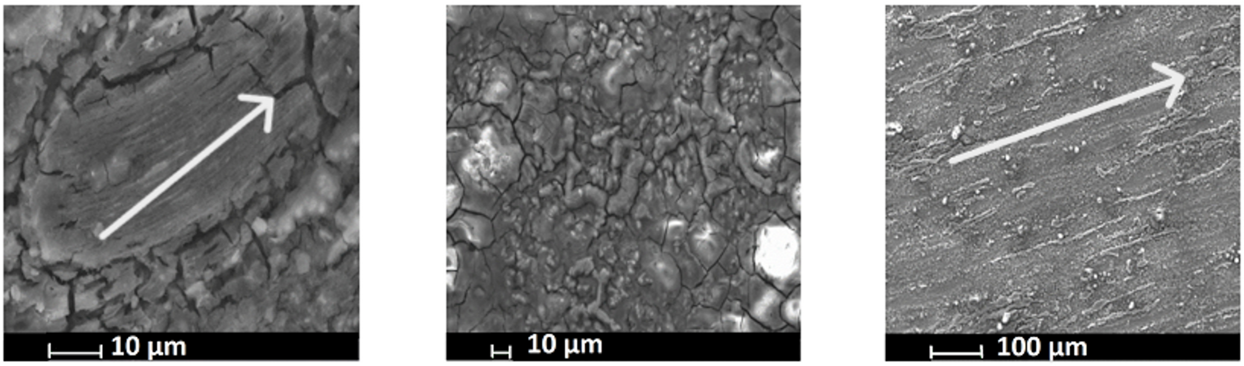

a b c

Fig. 1. SEM images of sample in initial state in longitudinal direction (arrow indicates extrusion axis) (a), samples after static compression at strain rate 0.1 s^{-1} in transverse section (b), in longitudinal section (arrow indicates compression axis) (c).

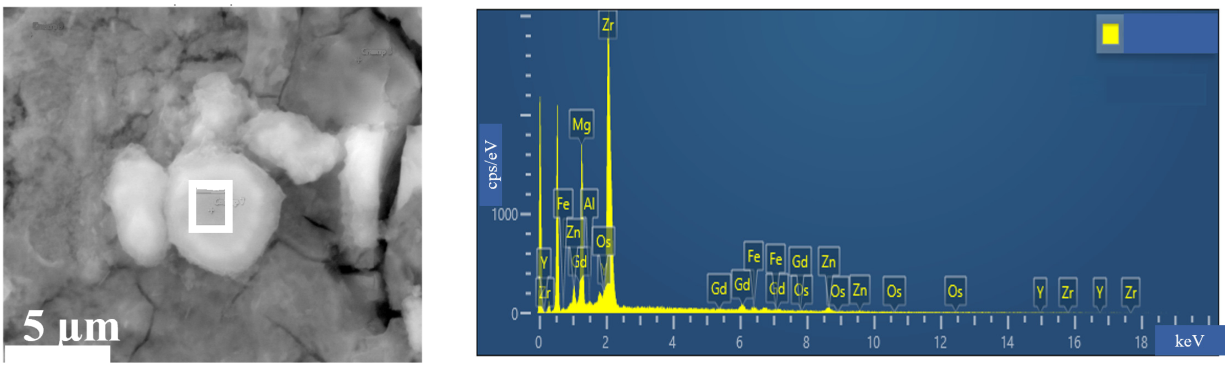

a b

Fig. 2. SEM image of sample after static compression at strain rate 0.1 s^{-1} in longitudinal direction (a), EDS data for the area selected in Fig. 2a for this sample (b).

fracture initiation region, Zr-rich intermetallic phases are repeatedly recorded, as well as, in some cases, phases with a high content of Y (up to 47.91%) and Gd (up to 29.31%).

Figure 4a shows microstructure of the sample after SHPB 2400 s^{-1} in transverse section.

In addition, at the highest loading rate of 5970 s^{-1}, local melting is observed (Fig. 4b). As for the Taylor test, the longitudinal section reveals features inherited from extrusion and modified by impact. The underlying lamellar LPSO phase, aligned with the extrusion/compression axis, remains clearly visible (Fig. 4c). Superimposed on this structure, slip bands inclined at an angle to the compression axis are observed, indicating active slip systems during deformation. The transition from the deformed to the undeformed part of the sample is gradual; in the undeformed region, the original extruded microstructure (with lamellar LPSO phase and equiaxed grains) is preserved with no signs of deformation-induced slip. Microcracks nucleate at a depth of about 50 nm with subsequent propagation to a thickness of 160 nm. Preserved initial eutectic components of the alloy are observed (Fig. 4d), but almost all of them are refined, twins are absent.

An analysis of the fracture surface reveals, that under static loading and at a strain rate of 2400 s^{-1}, a ductile-brittle fracture mechanism is typical (Fig. 5a, b): plateaus, steps, shear bands and local areas of this nature are observed. Dimples and cups are also encountered. For the sample after the Taylor test, stream and tree-like patterns, plateaus and steps, fracture by cleavage, as well as areas similar to local melting are observed (Fig. 5c).

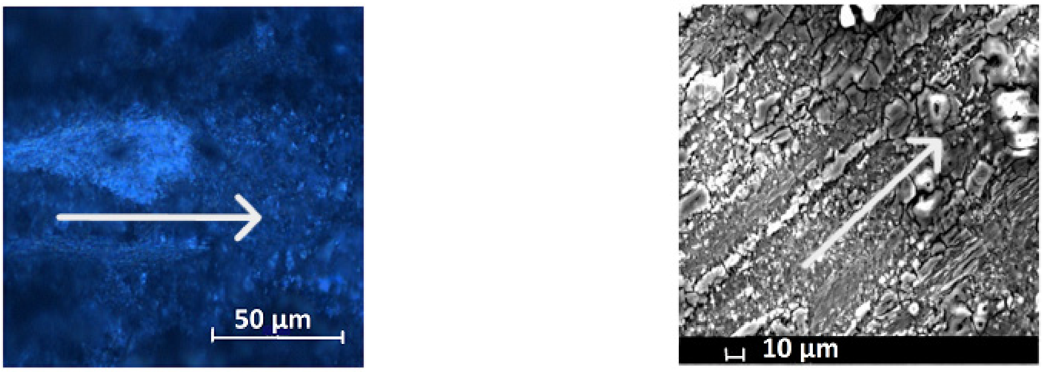

a b

Fig. 3. (Color online) C_DIC of sample after static compression at strain rate 0.001 s^{-1} (a), SEM image of sample after static compression in longitudinal direction at strain rate 0.1 s^{-1} (b). Arrow indicates compression axis.

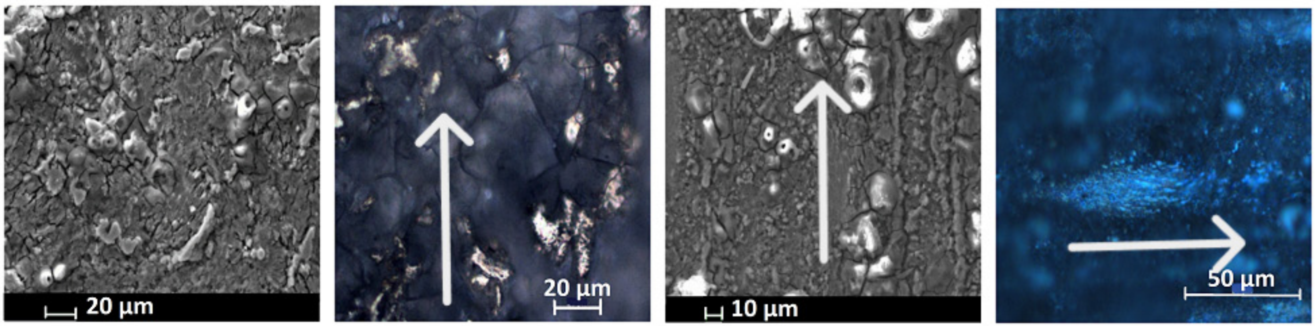

a b c d

Fig. 4. (Color online) SEM for sample after SHPB 2400 s^{-1} (a), optical for sample after SHPB 5970 s^{-1} (b), SEM for sample after Taylor test (c), C_DIC for sample after Taylor test (d). Arrow indicates compression axis.

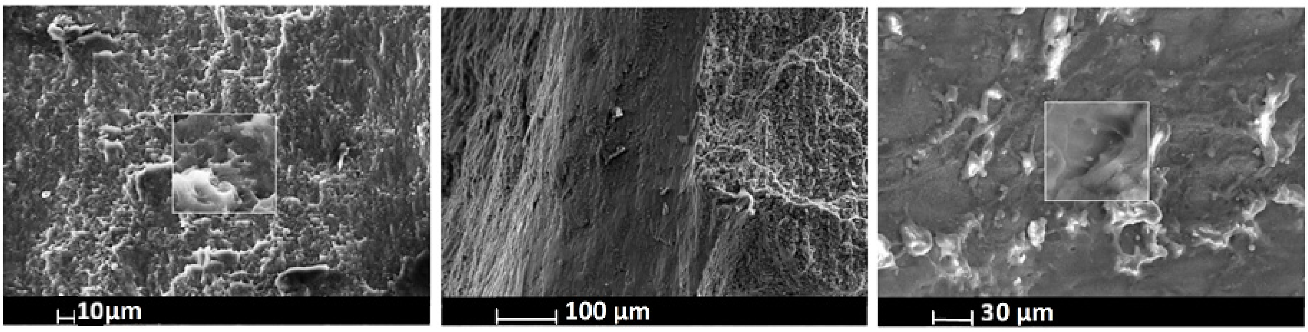

a b c

Fig. 5. Fracture surface for sample after static compression at strain rate 0.1 s^{-1} (in the insert the picture is enlarged 5 times) (a), after SHPB at 2400 s^{-1} (b), after Taylor test (in the insert the picture is enlarged 3 times) (c).

4. Discussion

After studying the microstructure photographs, a number of conclusions were made. In the longitudinal direction, the texture orientation is observed, which is caused by preliminary deformation — extrusion, as can be seen from Fig. 1c and 3 b. Also, there is a heterogeneity of grains — large eutectic initial grains and small ones formed during extrusion as a result of DRX, as, for example, in Fig. 1, 3 b, 4 a, 4 c. Most likely, areas with local Zr-rich intermetallic phases lead to local embrittlement, and Zr-rich intermetallic phases are usually observed at the crack initiation site, as in Fig. 1a, 4 a. With an increase in the strain rate, almost parallel cracks are observed in the samples characteristic of brittle fracture (Fig. 4 c).

Talking about the behavior of the sample microstructure after testing for the Taylor test, it can be noted that the slip lines are curved in the direction of preferential slip, which indicates the development of inhomogeneous plastic deformation. In the deformed parts of the samples, areas with fine grains are observed, which may be associated with both the occurrence of DRX during the Taylor test and the consequences of DRX during extrusion processing. As for the fracture surface, the revealed area and their surrounding microstructure at a quasi-static strain rate (Fig. 5 a) indicate the possible presence of localized Zr-rich intermetallic phases, but the relief prevents reliable identification of the chemical composition. With an increase in the strain rate, the nature of the fracture changes from ductile-brittle to predominantly brittle (Fig. 5 b). Also, after the Taylor test, local melting zones are observed, which is caused by a significant increase in the strain rate, which, in turn, leads to significant local heating (Fig. 4 c). Despite the melting zones, the fracture surface is also characterized by features of brittle fracture, such as stream patterns, cleavage facets, and river patterns. The presence of these features allows us to conclude that the proportion of brittle fracture increases with increasing strain rate.

Authors [28] examined Mg-4.7Gd-3.4Y-1.2Zn-0.5Zr sheets after unidirectional and cross rolling. They saw mixed fracture modes, with ductile tearing and micro-cracks near LPSO/second-phase areas, mainly at interfaces under stress. This aligns with our observation that the ductile part of the fracture surface decreases as the strain rate increases, pointing to a more brittle fracture. Similarly, in article authors [29] looked at Mg-8Gd-4Y-Zn-Zr alloys, extruded with and without bulk LPSO phases. They saw that bulk LPSO phases were linked to brittle fracture traits in some spots, especially around big second-phase particles. This backs up our idea that local embrittlement from Zr-rich intermetallic phases can start cracks and make brittleness worse at high strain rates.

After testing, the microhardness and average grain size were measured for all samples. The results are presented in Fig. 6, where the last right point is for the sample after Taylor test (the strain rate was calculated by approximation, Eq. (1)). Up to a strain rate of approximately 2000 s^{-1}, the microhardness increases, while the grain size decreases, and with a subsequent increase in the strain rate, the picture changes to the opposite: the microhardness begins to decrease, and the grain size increases. Only for the sample after the Taylor test are the highest values of both microhardness and grain size observed.

Probably, this type of dependence is caused by DRX occurring in the samples with an increase in the strain rate to 2000 s^{-1}, as well as presence of Zr-rich intermetallic phases at the grain boundaries, which contributes to an increase in hardness. With a subsequent increase in the strain rate, an increase in the number of cracks is observed, as well as the fracture of the samples. In addition, at high strain rates, local melting is observed (Fig. 4 b), followed by solidification in the form of large grain sizes where there were previously. This is also indicated by the segregations of Y and Gd, which are more refractory metals, which become noticeable at strain rates above 2000 s^{-1}. For the sample after the Taylor test, the increase in microhardness can be caused by a sharp increase in the number of dislocations at the impact site, as well as by the curvature of the LPSO phase at the impact site, which leads to local hardening.

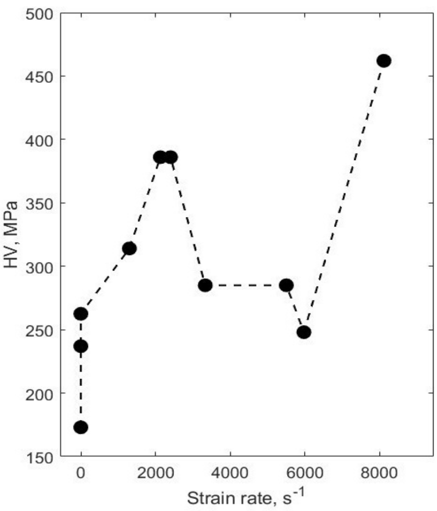

a

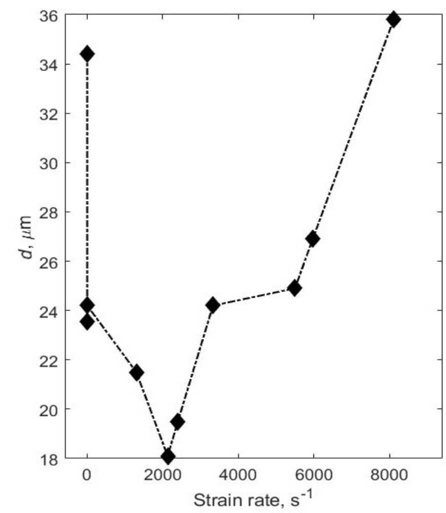

b

Fig. 6. The dependence of microhardness (a), and of average grain size (b) on strain rate.

The proportion of the viscous component (Shear area) in the fracture of material is presented in Table 1. From the presented data it is evident that with the growth of the strain rate the amount of the viscous component on the fracture surface decreases, i. e. the fracture becomes more brittle. This is also confirmed by the microstructural analysis.

Table 1. Shear area of the fracture surface for Mg-9Gd-4Y-1Zn-0.5Zr alloy.

NN	Method	Velocity	Shear area, %
1	Static compression test (Instron)	0.001 s^{-1}	87.6
2		0.001 s^{-1}	91.5
3		0.1 s^{-1}	91.9
4		0.1 s^{-1}	82.7
5	SHPB	2807 s^{-1}	77.7
6	Taylor test	219 m/s	49.5

5. Conclusion

This study investigates pre-extruded magnesium alloy in a wide range of strain rates.

The orientation of the structure of the samples in the longitudinal direction, caused by the preliminary deformation treatment, and refined eutectic components of the alloy, are noted in particular, after quasi-static tests. With an increase in the strain rate, areas with small grains are observed, which are the result of DRX. As the loading rate increases during tests on a Split Hopkinson Pressure Bar, the number of cracks increases; they become more branched, leading to the separation of the sample into parts, and local melting is also observed. The onset of crack formation usually starts at Zr-rich intermetallic phases, which are located near the grain boundaries and prevent grain growth of the material, but at the same time contribute to local embrittlement, especially with an increase in the strain rate.

The nature of the fracture changes from predominantly ductile to brittle with an increase in the strain rate. This is confirmed by data on shear area, despite the possible local heating, which entails melting and subsequent solidification with a large grain size.

The conclusions made about the microstructure are also consistent with the data on the microhardness of the samples and the value of their average grain size. At high strain rates above 5000 s^{-1}.

At high strain rates above 5000 s^{-1} (Hopkinson and Taylor test), the microhardness deviation from the trend predicted by the Hall-Petch law is observed, as its strengthening effect is overshadowed by other processes [30–32].

The authors believe that continuing studies on this promising alloy at higher strain rates 10^6–10^7 s^{-1} using a light gas gun would be of a great interest.

References

1. J.F. Nie, K.S. Shin, Z.R. Zeng, Microstructure, Deformation, and Property of Wrought Magnesium Alloys, Metall. Mater. Trans. A 51 (2020) 6045–6190.
2. L. Xiong, Z.S. You, S.D. Qu, L. Lu, Fracture behavior of heterogeneous nanostructured 316L austenitic stainless steel with nanotwin bundles, Acta Mater. 150 (2018) 130–138.
3. L. Xiong, Z.S. You, L. Lu, Fracture behavior of an austenitic stainless steel with nanoscale deformation twins, Scr. Mater. 127 (2017) 173–177.
4. X. Wu, Y. Wang, L. Qiao, J. She, F. Bi, Influence of Extrusion Ratio on Microstructure and Tensile Properties of Mg-Gd-Y-Zn-Zr Alloy, Metals and Materials International. 30 (2024) 2012–2022.
5. X. Wang, Y. Zhao, Y. Huang, Characterization of Hot-Extruded Mg-Gd-Y-Zn-Zr Alloy Containing a Novel Lamellar Structure and Related High Elevated-Temperature Mechanical Properties, Met. Mater. Int. 29 (2023) 2556–2570.
6. C. Xu, T. Nakata, G.H. Fan, X.W. Li, G.Z. Tang, L. Geng & S. Kamado, Microstructure and mechanical properties of extruded Mg-Gd-Y-Zn alloy with Mn or Zr addition, J. Mater. Sci. 54 (2019) 10473–10488.
7. Z. Ding, Y. Zhao, R. Lu, H. Pei, H. Hou, Microstructure evolution and mechanical properties of Mg-10Gd-3Y-*x*Zn-0.6Zr alloys, Journal of Materials Research 33 (2018) 1–9.
8. X. Yuan, Y. Du, D. Dong, D. Liu, B. Jiang, Corrosion Resistance Improvement of an Extruded Mg-Gd-Y-Zn-Zr-Ca via Aging Treatment, J. of Materi. Eng. and Perform. 31 (2022) 2909–2917.
9. L. Zhang, X. Wu, X. Zhang, X. Yang, Y. Li, Dynamic precipitation, dynamic recrystallization behavior, and microstructure evolution of the Mg-8.7Gd-4.18Y-0.42Zr alloy during hot deformation, J. Mater. Sci. 57 (2022) 20726–20745.
10. W. Liu, C. Zhang, Q. Shi, F. Han, P. Cao, Dynamic Recrystallization, Texture Evolution, and Improved Mechanical Properties of Mg-Y-Zn-V Alloy during Forging and Subsequent Extruding Deformation, Metals 14 (2024) 259.
11. Y. Yang, C. Mu, Z. Han, J. Xu, B. Li, Analysis of the In Situ Crack Evolution Behavior in a Solid Solution Mg-13Gd-5Y-3Zn-0.3Zr Alloy, Materials 14 (2020) 36.
12. S.Z. Wu, T. Nakata, G.Z. Tang, C. Xu, X.J. Wang, X.W. Li, X.G. Qiao, M.Y. Zheng, L. Geng, S. Kamado, G.H. Fan, Effect of forced-air cooling on the microstructure and age-hardening response of extruded Mg-Gd-Y-Zn-Zr alloy full with LPSO lamella, J. Mater. Sci. Technol. 73 (2021) 66–75.
13. Y.Q. Chi, C. Xu, X.G. Qiao, M.Y. Zheng, Effect of trace zinc on the microstructure and mechanical properties of extruded Mg-Gd-Y-Zr alloy, J. Alloy. Compd. 789 (2019) 416–427.
14. C. Xu, M.Y. Zheng, K. Wu, E.D. Wang, G.H. Fan, S.W. Xu, S. Kamado, X.D. Liu, G.J. Wang, X.Y. Lv, Effect of ageing treatment on the precipitation behaviour of Mg-Gd-Y-Zn-Zr alloy, J. Alloy. Compd. 550 (2013) 50–56.
15. C. Xu, T. Nakata, X. Qiao, M. Zheng, K. Wu, S. Kamado, Effect of LPSO and SFs on microstructure evolution and mechanical properties of Mg-Gd-Y-Zn-Zr alloy, Sci. Rep. 7 (2017) 40846.
16. M. Sun, D. Yang, Y. Zhang, L. Mao, X. Li, S. Pang, Recent Advances in the Grain Refinement Effects of Zr on Mg Alloys: A Review, Metals 12 (2022) 1388.

17. S. Zhang, M. Yang, F. Yuan, L. Zhou, X. Wu, Extraordinary fracture toughness in nickel induced by heterogeneous grain structure, Mater. Sci. Eng. A 830 (2022) 142313.
18. H. F. Li, J. L. Wei, S. P. Yang, Y. Q. Liu, The relationship between fracture toughness and tensile property in high-strength steels, Eng. Fail. Anal. 131 (2022) 105854.
19. Z. Ji, X. Qiao, L. Yuan, F.G. Cong, G.J. Wang, Mingyi Zheng, Exceptional fracture toughness in a high-strength Mg alloy with the synergetic effects of bimodal structure, LPSO, and nanoprecipitates, Scripta Materialia 236 (2023) 115675.
20. M. N. Antonova, S. Zhao, Yu. V. Petrov, M. Zheng, B. Li, Incubation-time-based modeling of the grain-size-influenced yield point phenomenon. Acta Mech. 235 (2024) 7141–7158.
21. S. Zhao, Yu.V. Petrov, Y. Zhang, G.A.Volkov, Z. Xu, F. Huang, Modeling of the thermal softening of metals under impact loads and their temperature–time correspondence, Int. J. of Engn. Science 194 (2024) 103969.
22. N. A. Kazarinov, Y. V. Petrov, A. V. Cherkasov, Instability effects of the dynamic crack propagation process, Engineering Fracture Mechanics 242 (2021) 107438.
23. S.A. Atroshenko, G.G. Savenkov, Evolution of the Microstructure of Obstacles from FCC Alloys Under High-Velocity Impact Conditions. In: H. Altenbach, V.A. Eremeyev, L.A. Igumnov, A. Bragov (Eds.), Deformation and Destruction of Materials and Structures Under Quasi-static and Impulse Loading. Advanced Structured Materials, vol. 186, 2023, Springer, Cham., pp. 19–27.
24. GOST 5639-82, Steels and alloys. Methods for detection and determination of grain size, State Committee of Standards of the USSR, Moscow, 1983. (in Russian)
25. ASTM E436-03 (Reapproved 2014), Standard Test Method for Drop-Weight Tear Tests of Ferritic Steels, ASTM International, West Conshohocken, PA, 2014.
26. W. Chen, B. Song, Split Hopkinson (Kolsky) Bar: Design, Testing and Applications, Mechanical Engineering Series, 2011, 390 p.
27. G. Taylor, The use of flat-ended projectiles for determining dynamic yield stress I. Theoretical considerations. Proceedings of the Royal Society of London. Series A, Mathematical and physical sciences 194 (1948) 1038.
28. Y. Han, Z. Chen, Y. Jiang, S. Jiang, Y. Gao, Y. Wan, C. Liu, Microstructure, deformation and fracture mechanism of Mg-Gd-Y-Zn-Zr alloy with different rolling routes during tension, Materials Science and Engineering: A 915 (2024) 147275.
29. D. Chen, T. Li, Z. Sun, Q. Wang, J. Yuan, M. Ma, Y. Peng, K. Zhang, Y. Li, Effects of Bulk LPSO Phases on Mechanical Properties and Fracture Behavior of As-Extruded Mg-Gd-Y-Zn-Zr Alloys, Materials 16 (2023) 7258.
30. S. A. Atroshenko, Local shear rate in different metals under dynamic loading, J. Phys. IV France 10 (2000) Pr9-231 – Pr9-236.
31. S. A. Atroshenko, Anomalous diffusion increase in steel under shock loading, J. Phys. IV France 110 (2003) 899 – 904.
32. S. A. Atroshenko, Martensite transformation in steels under impact load, J. Phys. IV France 112 (2003) 337 – 340.